designs

MDPI

Article

Mitigating Stress Shielding in Dorr C Femurs via Additive Manufacturing: A Proof-of-Concept Numerical Analysis

Roberta Cromi [1], Francesca Berti [1,*], Matteo Gavazzoni [2], Luigi La Barbera [1], Dalila Di Palma [1,2], Sara Maggioni [1,2], Jacopo Menini [3], Massimo Franceschini [3], Stefano Foletti [2] and Tomaso Villa [1]

[1] Department of Chemistry, Materials and Chemical Engineering—LaBS, Politecnico di Milano, Piazza Leonardo da Vinci 32, 20133 Milan, Italy; roberta.cromi@polimi.it (R.C.); luigi.labarbera@polimi.it (L.L.B.); dipalma.dalila2015@gmail.com (D.D.P.); sara.maggio97@gmail.com (S.M.); tomaso.villa@polimi.it (T.V.)
[2] Department of Mechanical Engineering—MetaMAT-Lab, Politecnico di Milano, Via La Masa 1, 20156 Milan, Italy; matteo.gavazzoni@polimi.it (M.G.); stefano.foletti@polimi.it (S.F.)
[3] Ortopedia e Traumatologia I, Istituto Ortopedico "Gaetano Pini", Piazza Cardinale Andrea Ferrari, 20122 Milan, Italy; jacopo.menini@asst-pini-cto.it (J.M.); massimo.franceschini@asst-pini-cto.it (M.F.)
* Correspondence: francesca.berti@polimi.it

Abstract

Bone resorption secondary to stress shielding is a leading cause of hip implant failure, primarily due to the stiffness mismatch between the femur and the prosthesis. Although anatomical stem designs generally provide improved load transfer, Dorr type C femurs often require straight stems to ensure adequate primary stability. This work presents a systematic approach to designing a straight, additively manufactured porous titanium hip stem aimed at minimizing stress shielding. The lattice architecture is customized to replicate the mechanical properties of bone based on patient-specific femoral CT scans. The performance of the resulting porous implant is numerically assessed under simplified physiological gait loading conditions. The implant behavior is evaluated through a homogenization strategy to model the lattice structure, significantly reducing the computational effort and making the methodology easily replicable. Compared to its full counterpart, the porous design achieves a significant reduction in predicted bone loss, suggesting that the proposed framework is a promising proof of concept for patient-specific implants. While further experimental validation and larger cohort studies are required, these findings highlight the potential of mechanically tunable porous structures to mitigate the stress shielding phenomenon in anatomical conditions such as Dorr type C femurs, which require straight stems.

Keywords: stovepipe femur; stiffness customization; lattice; patient-specific; finite element

Academic Editors: Richard Drevet and Antreas Kantaros

Received: 26 February 2026
Revised: 16 April 2026
Accepted: 20 April 2026
Published: 23 April 2026

1. Introduction

Total hip arthroplasty (THA) is among the most commonly performed joint replacement surgeries. Projections estimate a 176% increase in THA by 2040, rising to 659% by 2060 [1]. Although survival rates for hip prostheses are generally high, failures can still occur; clinical data from various countries [2–4] indicate that more than 30% of revision surgeries are due to aseptic loosening or periprosthetic fracture, which can result from excessive bone resorption. This issue can be attributed to non-optimal prosthesis design. Specifically, excessive stiffness mismatch between the femur and the prosthesis reduces the mechanical solicitation on the bone, leading to its loss: this phenomenon is known as stress shielding. Straight femoral stems are more prone to inducing bone resorption

compared to short or anatomical designs due to their bulkier geometry [5,6]; in cases of severe bone resorption, stem fracture may occur, as shown in Figure 1. Consequently, straight implants have been progressively replaced by fit-and-fill designs. Nevertheless, they remain a valuable solution in cases where anatomical shapes do not always lead to good postoperative outcomes, particularly in patients with a so-called stovepipe femoral canal, classified as Dorr type C [7,8].

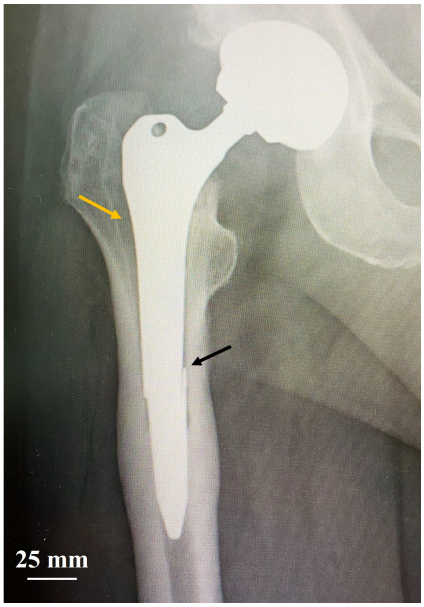

Figure 1. X-rays of a right THA failure in a Dorr type C femur as a consequence of stress shielding. The yellow lateral arrow indicates massive bone resorption in Gruen zone 1, while the medial black arrow indicates the stem fracture (image provided by Dr. Massimo Franceschini, orthopedic surgeon and head of Ortopedia e Traumatologia I, Istituto Ortopedico "Gaetano Pini").

The Dorr classification is based on the flare index (FI), defined as the ratio between the intracortical width of the proximal femur (20 mm proximal to the lesser trochanter) and the intracortical width of the canal isthmus: w_T/w_I (Figure 2) [9].

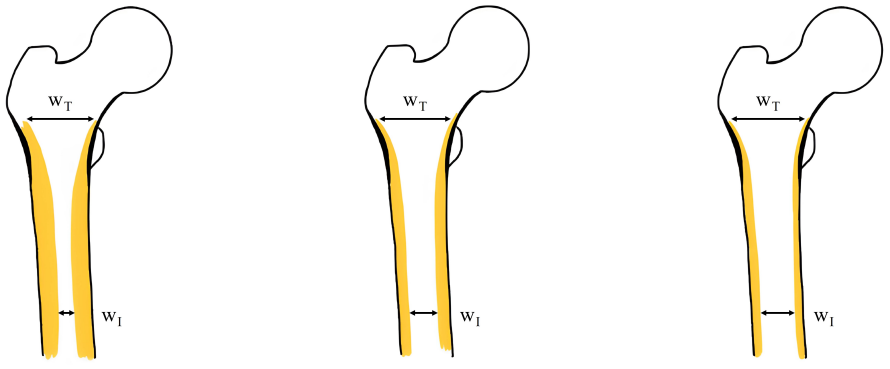

Figure 2. Dorr classification of the femur based on the flare index (FI), calculated as w_T/w_I. (**a**) Type A, "champagne-fluted" femur: $4.7 < FI < 6.5$; (**b**) Type B, "normal" femur: $3 < FI < 4.7$; (**c**) Type C, "stovepipe" femur: $FI < 3$.

In particular, stovepipe femurs are characterized by an FI lower than 3 and have a prevalence exceeding 10%, with a peak of 22% in the elderly population [7,10,11], mainly due to the progressive reduction in cortical thickness. In such cases, anatomical constraints significantly limit alternative options and straight stems—typically cemented—provide

better apposition to the femoral canal [12,13]. However, the implantation of bulk straight stems, designed for distal fixation within the femoral canal, can lead to proximal loosening. This phenomenon, in conjunction with the thin cortical layers, increases the susceptibility to aseptic failure, resulting in a periprosthetic fracture incidence of 15.9% [7]. To address the surgical requirement for a straight stem while mitigating the phenomenon of stress shielding, a design strategy aimed at tailoring the stiffness of the prosthesis to match that of human bone and control bone resorption/regrowth could potentially reduce the incidence of THA failures [14].

In this context, additive manufacturing (AM) has opened up unprecedented opportunities over the last decade, including the ability to customize the mechanical properties of solid materials by controlling the mesoscale porosity [15,16]. The use of lattice structures and cellular materials, fabricated from a wide range of constitutive materials, has led to improved component performance across various fields [17].

Specifically, in the orthopedic sphere, significant improvements can be achieved through the development of metamaterials composed of biocompatible metals (e.g., titanium alloys) exhibiting elastic properties comparable to those of human bone [18–24]. AM's ability to produce complex and unique shapes without additional costs or setting times represents a driver in the realization of high-performance patient-specific devices [25,26]. Customized prostheses are becoming an effective solution, as they can provide optimized performance and mimic the organic nature of native bone, enhancing their integration with the surrounding tissue [27].

The application of lattice structures in THA to reduce stem stiffness, and consequently stress shielding, has been extensively investigated in the literature. The most common approach involves tailoring the lattice geometry to achieve a stem with a spatially varying stiffness distribution [28–30]. Although these studies provide valuable insights into the mechanical potential of lattice-based designs, they do not explicitly analyze the potential mitigation of the stress shielding phenomenon [28,30], or they rely on simplified synthetic femur configurations [29]. More recent studies have incorporated patient-specific bone geometries derived from computed tomography (CT) scans. In particular, Alkhatib et al. [31] and Nomura et al. [32] directly guided stem design by optimizing the spatial distribution of porosity (or relative density) to tailor the implant stiffness according to the stress distribution in the native femur. By contrast, Gok et al. [33] and Kladovasilakis et al. [34] employed imaging data only for the evaluation of bone loss, without tailoring the implant design, thereby limiting the potential for stress-adaptive optimization. Arabnejad et al. [35] adopted a different strategy, introducing a graded lattice structure based on the bone density distribution derived from CT scans. Although this approach enables a biomimetic design, the use of homogenization in the presence of a graded architecture may compromise the accuracy of the results, as the homogenized scale separation assumption necessitates the sufficient repetition of identical unit cells. Limmahakhun et al. [36] developed a stem featuring both longitudinally and radially varying stiffness by properly tuning the pillar thickness of octahedral cells; however, as previously mentioned, the radial partition of the stem may compromise the accuracy of the results when using a continuous approach due to the reduced dimensions of the sections. By contrast, Naghavi et al. [37] proposed a detailed analysis of their hip prosthesis design, in which stiffness distribution was guided by the stress field resulting from the operating loading conditions. While this strategy avoids the limitations related to the homogenization theory, a highly detailed numerical model comprising over 20 million nodes is required, with a large computational cost.

While these studies highlight the potential of lattice-based designs to tailor implant stiffness, significant limitations remain. Approaches based on fully resolved lattice geometries or multi-scale modeling can provide higher fidelity in capturing local mechanical

behavior, but they are often associated with extremely high computational costs, limiting their applicability in a clinical or preoperative planning context. For instance, detailed models may require tens of millions of elements and the use of high-performance computing resources, making them impractical for routine use. Conversely, simplified approaches based on linear elastic homogenization significantly reduce the computational effort but rely on strong assumptions, such as scale separation and periodicity of the unit cell, which may not be fully satisfied in graded or patient-specific designs. Moreover, most existing studies adopt linear material behavior and simplified bone remodeling models, neglecting non-linear bone responses and time-dependent adaptation mechanisms, which may affect the accuracy of long-term predictions.

In this context, the present solution positions itself as a trade-off between model fidelity and computational efficiency, proposing a systematic and clinically feasible framework that leverages homogenization while explicitly acknowledging its limitations. The aim is not to provide a fully predictive model of bone remodeling but rather a robust and reproducible tool for the comparative design and preliminary assessment of a load-sharing customized lattice hip implant specifically tailored to the biomechanical needs of Dorr type C femoral bone. Given the critical issue of stress shielding, particularly in similar cases, where clinical constraints require the use of a straight stem, the framework focuses on (i) reconstructing and analyzing anatomical data to accurately capture the bone density distribution; (ii) minimizing peri-prosthetic bone loss, compared to a solid stem counterpart, through an optimal lattice structure distribution; and (iii) ensuring computational efficiency, compatible with preoperative surgical planning.

2. Materials and Methods

2.1. Bone Reconstruction

Femur CT scans of a patient cohort were provided by Prof. Innocenti, PhD (Université Libre de Bruxelles, Bruxelles, Belgium), among which a dedicated Dorr-C healthy adult male case was identified. The geometry of the femur was reconstructed from the DICOM data using the commercial software Mimics 25.0 (Materialise NV—Leuven, Belgium) to create an FE model in Abaqus 2022 (Dassault Systèmes SIMULIA Corporation—Johnston, RI, USA).

Beyond geometry definition, CT scans were used to map the elastic modulus field in the bone by means of literature correlations between the gray scale of the CT and the elastic modulus of the portion of bone corresponding to a voxel, using the open-source software Bonemat v3.2 (Istituto Ortopedico Rizzoli—Bologna, Italy) [38]. Specifically, the software requires as input the CAD format of the bone and the CT scan images, and, once the parameters needed for the correlation are chosen, it generates an FE model (Abaqus input file) where each tetrahedral element has a specific elastic modulus value. In the absence of specific calibration data, the CT scan grayscale values (expressed in Hounsfield units, HU) were associated with the local bone elastic modulus E through a set of literature-based equations (Equations (1)–(3)) specific for the proximal femoral region:

$$\rho_{QCT} = -0.00393573 + 0.000791701 \cdot HU \quad (1)$$

$$\rho_{ash} = 0.079 + 0.877 \cdot \rho_{QCT} \quad (2)$$

$$E = 0 + 14,664 \cdot {\rho_{ash}}^{1.49} \quad (3)$$

where ρ_{QCT} is a value representative of the bone mineral density, while ρ_{ash} is the physical quantity relating the bone mineral density to the bone mechanical properties [39]. With different elastic modulus values (E) associated with each element, a mesh sensitivity

analysis was performed. Edge lengths from 2 mm to 6 mm across six distinct femoral zones were evaluated; for each region, the average E—weighted by the element volume—was calculated and compared against the results obtained from the finest mesh.

2.2. Prosthesis Design

The prosthesis CAD model used in this work was designed in Solidworks 2020 (Dassault Systèmes—Vélizy-Villacoublay, France) (Figure 3a), mimicking the design of a commercially available straight, tapered solution with a rectangular cross-section. In order to satisfy the stringent constraints required for correct THA positioning, the prosthesis was properly sized and placed inside the femur (Figure 3b) using Materialise 3-matic (Materialise NV—Leuven, Belgium) under the supervision of orthopedic surgeons (M.F. and J.M.).

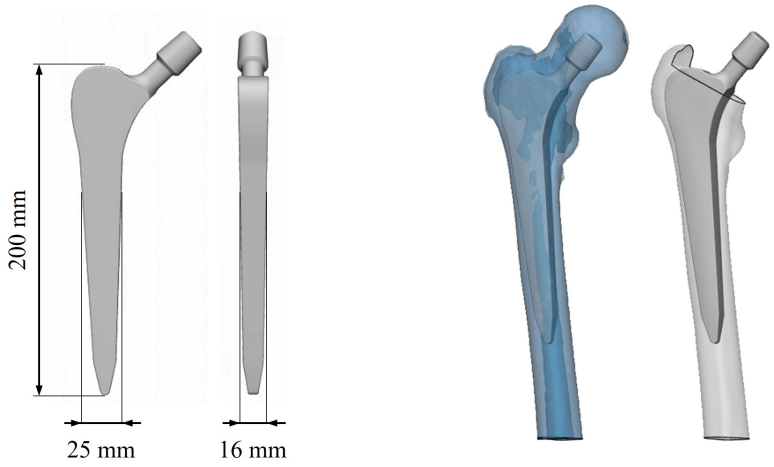

(**a**) 3D CAD geometry (**b**) Positioning in the femur

Figure 3. Prosthesis design inspired by a commercially available straight stem.

The placement of the prosthesis allowed the identification of the bone portions removed during THA. As previously mentioned, in order to reduce stress shielding, an ideal prosthesis should exhibit mechanical behavior equivalent to that of the replaced bone. To this aim, the distribution of E was mapped onto the bone volume occupied by the stem using Bonemat, following the same procedure previously described for the femur model. Subsequently, the internal filling of the prosthesis was defined by modulating the density of the lattice structure. As homogenization cannot be reliably applied to graded lattice structures, a periodically repeated lattice over sufficiently large volumes was adopted, rather than a graded configuration in which each unit cell potentially differs from the others [40,41]. This approach significantly reduces the computational costs while providing accurate approximation of the overall mechanical response of the implant [42]. The choice of four longitudinal regions was not arbitrary but resulted from a trade-off between the spatial resolution and the requirements of the homogenization approach. The initial number of partitions was set equal to thirty; in each zone, the homogeneous elastic modulus was computed as the volume-weighted average of the elastic moduli of all elements whose center of mass belonged to the respective partition. However, it is important to note that, in order to satisfy the homogenization assumption of infinite periodicity, the region characterized by a uniform lattice geometry should be sufficiently large to ensure consistent results [43,44]. Consequently, adjacent regions with comparable elastic moduli were merged, resulting in a stem that was transversally partitioned into four sub-regions based on the average bone E computed from the corresponding superimposed CT regions along the femoral axis.

The most suitable 3D cell capable of guaranteeing mechanical properties consistent with bone was selected from the library of nTop 3.40 (nTopology—New York, NY, USA) after preliminary analyses, following two main directions:

1. The lattice cell had to guarantee an adequate value of E but, at the same time, high fatigue strength, so the ratio between these two quantities was investigated;
2. The lattice cell had to have a morphology with feature dimensions compatible with the current technological limits for laser power bed fusion processes so as to ensure manufacturability.

Once selected, the lattice cell was mechanically characterized in terms of the equivalent homogenized E, which depends on three main parameters: the base material E_s, the topology, and the relative density ρ^*, defined as the density of the lattice ρ over the density of the corresponding solid material ρ_s. For full characterization, 4 cells with different ρ^* were generated to obtain Ashby maps for the homogenized E [45,46]. First, the relation between ρ^* and the strut thickness (t) over the cell length (L) was evaluated; second, the link between ρ^* and the ratio between a given homogenized mechanical property of the lattice and the corresponding property of the base material [45,46] was investigated. The relation between ρ^* and E was found by adopting linear elastic homogenization theory and simulating a single cell with periodic boundary conditions (PBC).

By considering the target values of E derived from the CT analysis, the corresponding ρ^* values were computed by reversing the relationship of E. Subsequently, the ratios t/L were obtained based on ρ^*. To ensure that the minimum t of the strut in all four regions exceeded 300 μm, which was considered a reasonable technological limit for the smallest printable features [21], the cell length was set to 2 mm. The prosthesis was filled with the selected unit cell by means of the software nTop, in which continuity among the four different domains was ensured by imposing a linear variation in the strut t over a distance of 2 mm.

2.3. Stress Shielding Performance Evaluation

The evaluation of stress shielding performance is of primary importance to properly design a hip implant. Specifically, in this study, stress shielding was investigated through static linear numerical analyses, as proposed in several literature works [20,21,35,37,47,48]. FE analyses were performed on the intact physiological bone, which served as the reference, and on the implanted bone, considering both a fully solid titanium implant and the novel lattice-based design proposed here (all simulations were run on 32 cores on a computing node equipped with 125 GB RAM).

The research was carried out under simplified loading conditions representative of the physiological gait, as schematically illustrated in Figure 4a. Specifically, the applied loads included the hip joint reaction force (F_1), the contribution of the abductors (F_2), the tensor fasciae latae (F_3, F_4), and the vastus lateralis (F_5), as these muscles are known to have the greatest influence on the femural stress field [49,50]. The magnitudes and 3D orientations of these forces (Table 1) were taken from the literature [47] and represent the effective loads acting on the femur of an 85 kg individual during the peak loading phase of walking (single-leg stance). Since this study was conceived as a proof-of-concept investigation based on a single patient, such a body weight was adopted as a representative average value for an adult male, consistent with the CT data used for femoral reconstruction.

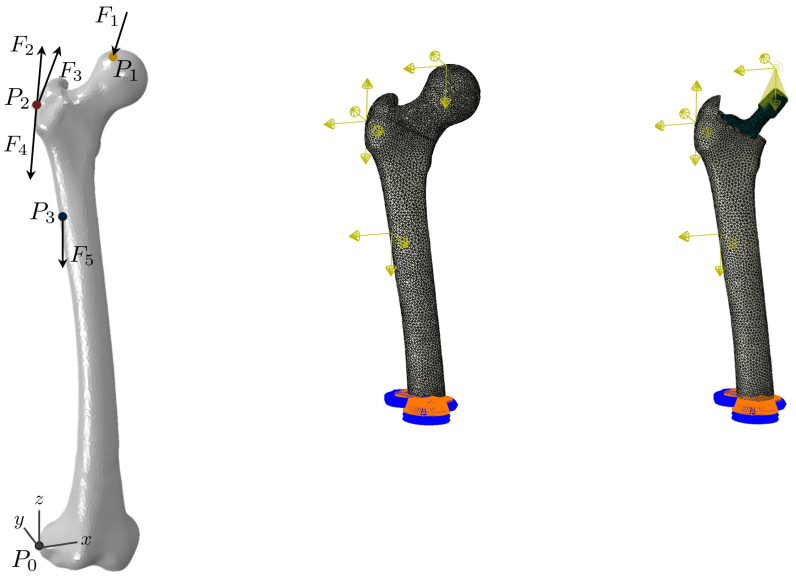

(**a**) (**b**) (**c**)

Figure 4. FE models used for evaluation of stress shielding: (**a**) forces acting on the femur in physiological conditions (for numerical values, see Table 1); (**b**) FE model for intact femur; (**c**) FE model of implanted femur.

Table 1. Effective forces acting on the femur of a human weighing 85 kg at a maximum load while walking (single-leg stance). The directions of the forces are coherent with the coordinate system reported in Figure 4a.

Force	F_x **[N]**	F_y **[N]**	F_z **[N]**
Hip contact (F_1)	−451	268	−1916
Abductor (F_2)	485	−36	723
Tensor fascia latae (F_3)	60	−97	110
Tensor fascia latae (F_4)	−4	6	−159
Vastus lateralis (F_5)	−8	−155	−777

To computationally simulate the physiological bone, FE analyses were performed on the Bonemat-based model obtained from CT scan reconstruction (Figure 5a), which was previously used to derive the E design targets. The model consisted of tetrahedral elements; to expedite the analyses and reduce the computational costs, linear elements were adopted, as no particular emphasis was required to address local stress concentrations. The loads acting on the femur were applied as concentrated nodal forces, as shown in Figure 4b, coupled with a femoral portion equivalent to the area of muscle attachment. Since the interest was focused on the region potentially affected by the implant, only the proximal femur was considered in the analysis; the distal end of the bone was fully constrained in all three directions to prevent rigid body motion (Figure 4b,c), in agreement with the literature [36,37].

The implanted femur was modeled as two separate solid parts:

1. Implanted bone—similarly to the intact bone, an FE model was generated with Bonemat
2. Implanted prosthesis—a stem composed of 5 materials was designed. An isotropic material with the E of titanium (110 GPa) was assigned to the neck region, whereas four distinct orthotropic materials were used for the lattice regions, with elastic properties obtained through linear elastic homogenization.

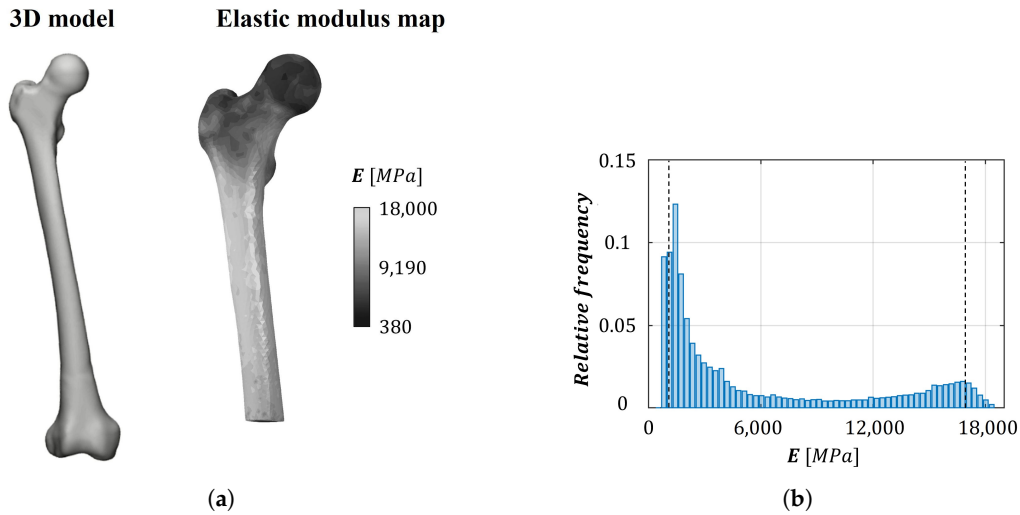

Figure 5. Femur reconstruction for numerical models: (**a**) 3D reconstruction and elastic modulus color map; (**b**) histogram of the elastic modulus distribution obtained through Equations (1)–(3), where vertical reference lines at 1 GPa and 17 GPa correspond to typical values of trabecular and cortical bone elastic moduli, respectively.

The applied loads were identical to those used for the intact femur, except for the hip joint reaction, which was applied by means of a reference point rigidly coupled to the implant head (Figure 4c). In this way, it was possible to emulate the presence of the acetabular cup, preserving the position of load application. Regarding the interaction between the two parts, a tie was adopted, i.e., the two surfaces in contact were rigidly connected under the hypothesis of complete osseointegration, symbolizing an idealized yet representative long-term condition [51].

Once the stress and strain fields of both the intact and implanted femurs were obtained from the FE analyses, the stress shielding performance of the designed porous implant was evaluated by comparing the solicitation into the native bone. An adaptive bone remodeling process occurs whenever the bone stimulus pattern is altered by an unnatural loading condition, as may happen in the presence of a hip prosthesis. To assess this phenomenon, the simplified model proposed by Frost [52,53] and widely adopted in the literature for hip implant evaluation [35,37] was employed. This model relates stress shielding to variations in the strain energy U to which the bone is subjected. Bone tissue can be considered locally underloaded when the strain energy per unit of bone mass ($S = U/\rho$, where ρ is the local bone density in g/cm^3) falls below a reference value S_{ref}, corresponding to S in the case of an intact femur.

However, not all underloading conditions lead to resorption, since a certain tolerance range—referred to as the *dead zone*—is physiologically acceptable. Bone resorption is assumed to occur when the local value of S is beneath the value of $(1 - s) \cdot S_{ref}$. In accordance with the literature, the dead zone parameter was set to $s = 0.75$ [35], indicating that a given region of bone is prone to resorption when the strain reduction after implantation exceeds 25% relative to the intact femur (under the assumptions of a linear elastic material and uniaxial load). Conversely, bone regrowth is expected when $S > (1 + s) \cdot S_{ref}$, which corresponds to a strain increase greater than 175% of the original value under the hypothesis of uniaxial loading. Under these assumptions, the bone remodeling rate $d\rho/dt$, i.e., the temporal evolution of bone density, can be described as

$$\frac{d\rho}{dt} = \begin{cases} > 0, & when \;\; S > (1+s) \cdot S_{ref} \\ = 0, & when \;\; (1-s) \cdot S_{ref} \leq S \leq (1+s) \cdot S_{ref} \\ < 0, & when \;\; S < (1-s) \cdot S_{ref} \end{cases} \quad (4)$$

Bone remodeling is a local volumetric phenomenon; therefore, it was assessed by comparing the strain energy values resulting from the FE models of the prosthetic femurs, implanted with both solid and porous stems, with those of the intact femur, which served as the reference configuration. In particular, elements exhibiting strain energy values lower than $1 - s$ of the reference were classified as prone to resorption, while those with strain energy values above $1 + s$ were considered prone to regrowth. Finally, the total resorbed and regrown masses were computed by summing the masses of the corresponding elements, obtained considering the initial bone density.

3. Results and Discussion

3.1. Bone Reconstruction

The 3D model of the femur and the corresponding map of E are shown in Figure 5a, while the related histogram of the observed E values is reported in Figure 5b. The sensitivity analysis performed on the bone element size, aimed at ensuring accurate Young's modulus assignment, indicates that no significant differences occur in either the modulus map or the histogram for elements with an edge length of 4.5 mm or less. Accordingly, an element size of 4 mm was selected for modeling the bone ($error < 1.5\%$) and has been kept constant throughout the study. Upon analyzing the histogram, it is possible to observe that it covers a range of E that is consistent with the literature, with peaks at approximately 1 GPa and 17 GPa, corresponding, respectively, to trabecular and cortical bone [33,54].

3.2. Prosthesis Design

The anatomical model replicates the intraoperative conditions of a THA procedure, ensuring the proper resection of the femoral head and the preservation of the greater trochanter. The Young's modulus distribution resulting in the femoral region where the stem is implanted is reported in Figure 6a. Each bar of the histogram shown in Figure 6b represents the average value over the corresponding stem section. The figure highlights the four identified portions, within which E exhibits limited variability. On the right side of the histogram, a schematic representation of the partitioned prosthesis is provided, together with the corresponding values of E, which serve as design targets. Taking into account the goal of stress shielding minimization, the optimal solution consists of a femoral stem filled with three-dimensional graded lattice structures that replicate exactly the Young's modulus distribution of the removed bone portion (Figure 6b,d).

The selected unit cell is a strut-based diamond lattice, which is widely used in the literature regarding bone replacement lattices due to its elastic isotropy, low stiffness, and high strength [55]. The mechanical characterization of the unit cell results in two different equations able to describe the structure's behavior.

- As studied in the literature [46], the relationship between ρ^* and the ratio between t and L is identified. The following relation is obtained by fitting the data of the four selected cells:

$$\rho^* = \frac{\rho}{\rho_s} = 3.35\left(\frac{t}{L}\right)^{1.83} \quad (5)$$

- The relation between ρ^* and the ratio of E to the base material modulus, derived from the mechanical characterization of the cell, is also found to follow a power law:

$$\frac{E}{E_s} = 0.71(\rho^*)^{2.14} \quad (6)$$

The prosthesis filled with the diamond lattice is shown in detail in Figure 6d. The zoomed-in details allow us to appreciate the different structures used to achieve the various target Young's moduli; the corresponding values of ρ^* are also reported.

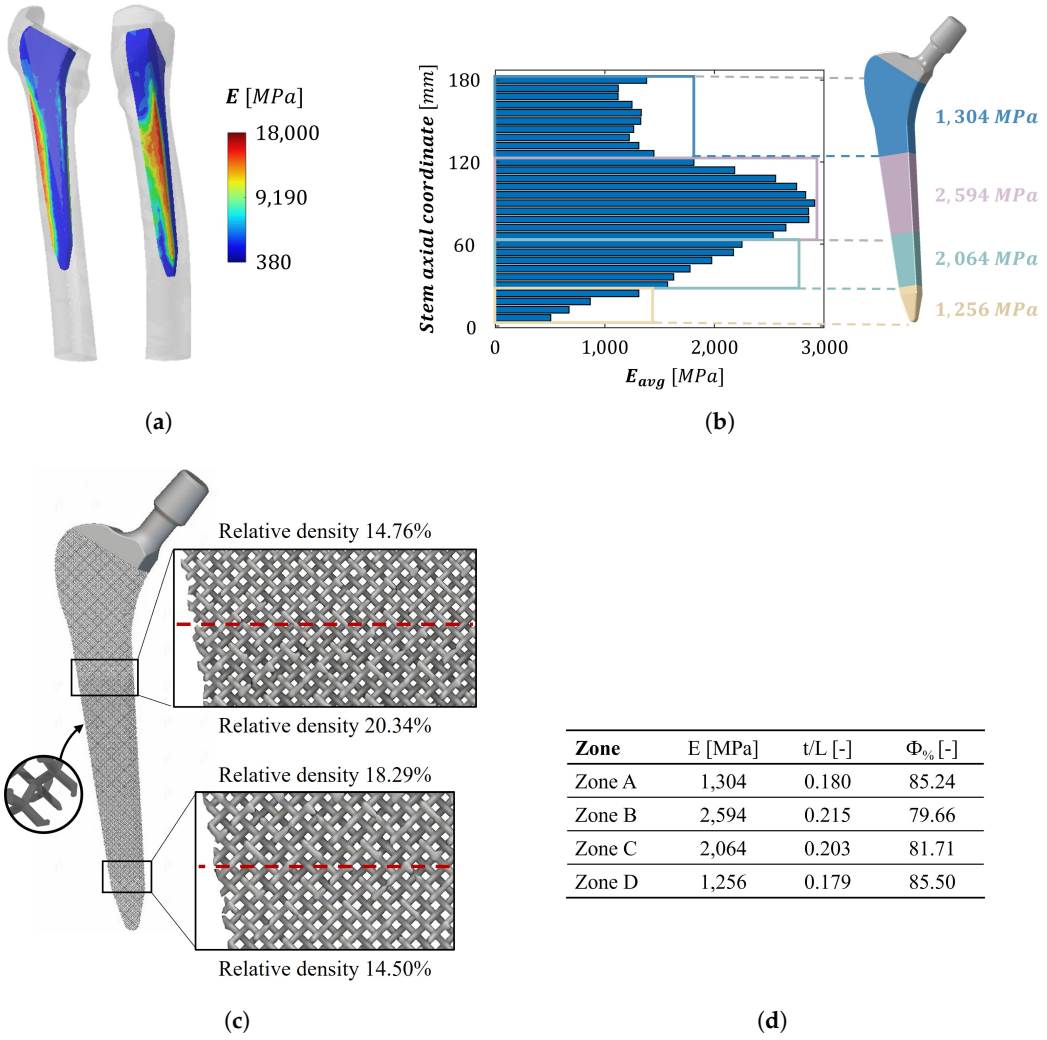

Zone	E [MPa]	t/L [-]	$\Phi_{\%}$ [-]
Zone A	1,304	0.180	85.24
Zone B	2,594	0.215	79.66
Zone C	2,064	0.203	81.71
Zone D	1,256	0.179	85.50

Figure 6. Prosthesis design against stress shielding: (**a**) ideal distribution of elastic modulus on the stem reconstructed from patient CT scans; (**b**) discretization of the ideal elastic modulus distribution and subdivision of the stem in iso-stiffness regions; (**c**) lattice stem design exploiting a diamond strut-based cell with different relative densities; (**d**) elastic modulus, cell thickness-to-length ratio, and porosity value for each zone, ordered from the proximal portion to the distal end of the stem.

In this configuration, the pore size of the selected unit cell exceeds the optimal range for bone ingrowth ($p_{required}$ < 800 µm). The application of an external porous coating could mitigate this issue and improve osseointegration. Nevertheless, the impact of such modifications on the overall mechanical performance should be quantitatively evaluated. Specifically, while it has been demonstrated [56] that the addition of an external coating characterized by semi-spherical pores and cylindrical cell development channels does not affect the fatigue performance of the femoral stem, the presence of an external layer in direct contact with the surrounding bone would inevitably influence the femur–implant

load transfer. Such a modification could alter the ability of the stem to mitigate the stress shielding phenomenon. Furthermore, design modifications involving variations in pore size and lattice geometry, including TPMS structures, may be investigated with the aim of enhancing osseointegration and improving secondary stability [57].

3.3. Stress Shielding Performance Evaluation

A comparative FE analysis between intact and implanted bone models provides a quantitative basis on which to evaluate the resulting bone remodeling process. In Figure 7a, the maximum principal strain maps are reported for the three configurations (a section view is provided for each case). The femur implanted with the porous implant exhibits a strain distribution consistent with the physiological conditions. In contrast, the fully dense titanium implant leads to pronounced underloading in both regions highlighted by the rectangles. The amounts of bone resorption and bone apposition predicted for the simil-bone implant are compared with those of the fully solid implant in each Gruen zone in Figure 7b. Total bone resorption of 34% and <1% is predicted for the fully solid and porous implant configurations, respectively, under the assumptions of the present model. While these values suggest a substantial reduction in the stress shielding effects with the porous design, they should be interpreted as indicative of relative trends rather than as precise quantitative predictions. More specifically, the porous prosthesis shows limited predicted bone loss, primarily localized in the proximal region (Gruen zone 7), whereas the fully solid implant exhibits more extended resorption patterns, affecting both proximal and distal regions (notably Gruen zones 6, 7, 1, and 2). On the other hand, the ideal implant exhibits bone regrowth mainly in the proximal region, particularly in Gruen zones 1 and 7 (Figure 7b). Overall, the model assumptions may lead to the overestimation of the predicted reduction in stress shielding, as idealized interface conditions and linear material behavior tend to promote more uniform load transfer between the implant and bone. These results qualitatively indicate that the porous configuration promotes more physiological load transfer compared to the fully solid counterpart.

Additionally, it should be considered that, by combining controlled lattice architectures with patient-specific anatomical data, the implant ensures adequate primary stability. From a clinical perspective, these kinds of porous implants allow surgeons to avoid the use of bone cement. This aspect is particularly relevant considering both the complications associated with cement failure and the limited suitability of cemented fixation in patients with significant comorbidities (e.g., cancer, advanced age, severe cardiopulmonary disease, or osteoporosis) due to the increased risk of developing bone cement implantation syndrome, which may lead to severe symptoms, potentially culminating in cardiac arrest [58–60].

It is worth noting that this simplified model cannot completely represent the actual bone remodeling process, as it neglects the time-dependent nature of the phenomenon and the biological mechanisms. Equation (4) provides only an estimate of femur portions that may be prone to resorption/regrowth in the immediate postoperative condition and does not predict long-term evolution. For this reason, bone loss and regeneration were evaluated based on variations in U rather than in S, since ρ variations were not explicitly modeled. More sophisticated bone remodeling algorithms, such as the one developed by Huiskes et al. [61], combined with a dynamic dead zone parameter and the simulation of cyclic loading conditions, could improve the prediction of the long-term evolution of bone regrowth/resorption. Nevertheless, the effectiveness of the methodology implemented in the present study is not compromised within a comparative framework.

Additional aspects should also be addressed. First, a solid distal end should be introduced to ensure surgical compatibility and prevent lattice damage during stem implantation. Furthermore, fatigue analyses under physiological loading conditions (e.g., gait

and stair climbing) should be performed to assess long-term mechanical reliability. In this context, numerical simulations involving homogenization approaches significantly reduce the computational cost (a few hours for the entire analysis, from homogenization to bone loss evaluation) compared to detailed porous models [37]. However, they do not capture local stress concentrations within the lattice structure, which may affect the accuracy of the predicted mechanical response, enabling only the preliminary identification of potentially critical regions. These should subsequently be investigated in detail through submodeling techniques and validated via experimental analysis. Finally, to enhance the robustness and generalizability of the findings, future studies should include a sensitivity analysis and consider expanding the dataset by including a larger cohort of patients.

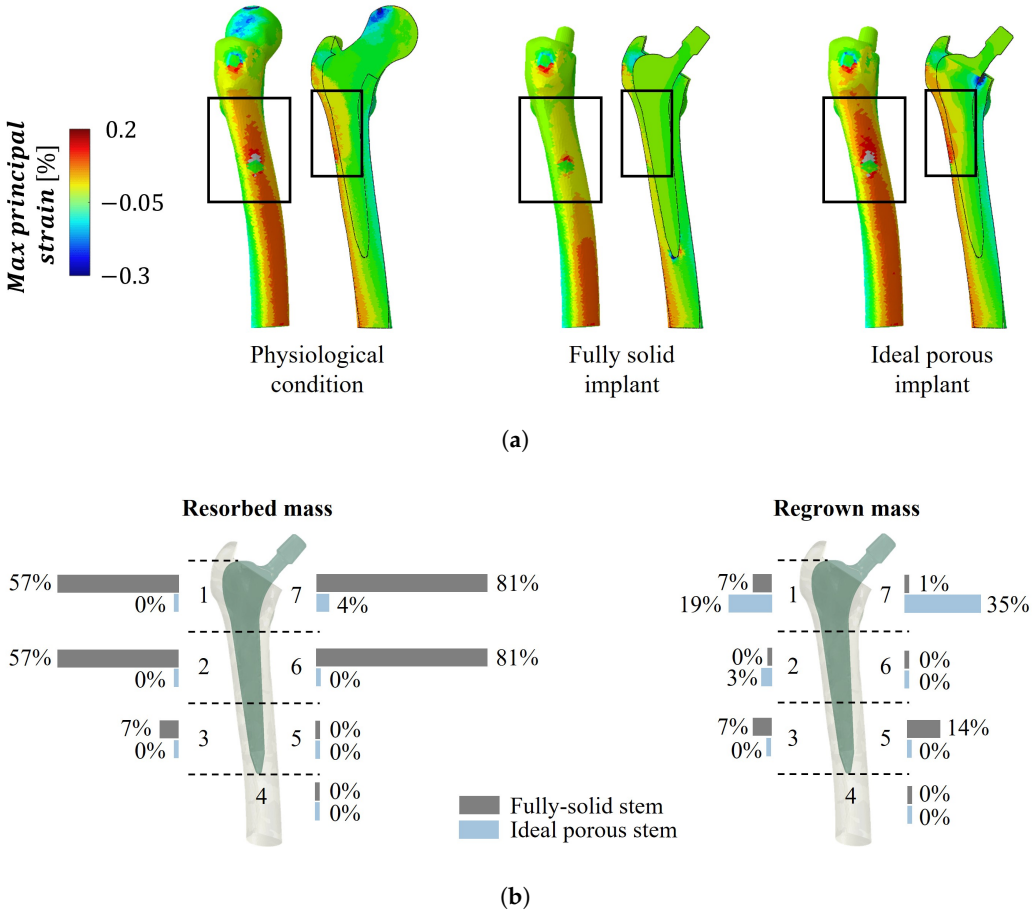

Figure 7. Stress shielding performance evaluation. (**a**) Maximum principal strain map for intact bone, bone implanted with a fully dense titanium implant, and bone with the porous lattice implant; the rectangles highlight the regions of pronounced underloading for the fully dense titanium implant. (**b**) Resorbed and regrown mass evaluations in the Gruen zones 1–7.

4. Conclusions

A systematic methodology to tailor the stiffness of a hip prosthesis is presented, based on CT images of a patient with a Dorr type C femur. The proposed framework, employing AM technologies, enables the design of an uncemented, porous, straight stem specifically optimized for the Dorr C femoral morphology, achieving a significant reduction in predicted bone loss compared to the fully solid counterpart. Moreover, the design of a patient-specific porous implant ensures adequate primary stability while potentially avoiding the use of bone cement, which is particularly advantageous for patients with significant comorbidities.

While these results are promising, it is important to acknowledge that this study serves only as a proof-of-concept work and carries limitations. The current model neglects the complex, time-dependent nature of bone remodeling, focusing on the immediate postoperative condition. Therefore, fatigue analyses, experimental validation, and the inclusion of a larger patient cohort will be pursued, as they are necessary steps to confirm the clinical scalability of the methodology and to assess the long-term mechanical reliability of porous femoral stem designs, as well as for future regulatory approval.

Author Contributions: Conceptualization, S.F. and T.V.; methodology, S.F., T.V., F.B., L.L.B., and M.G.; software, R.C., F.B., M.G., D.D.P., and S.M.; validation, J.M., M.F., and T.V.; formal analysis, R.C., F.B., M.G., D.D.P., and S.M.; investigation, R.C., F.B., M.G., D.D.P., S.M., and T.V.; data curation, R.C. and F.B.; writing—original draft preparation, R.C., F.B., M.G., D.D.P., and S.M.; writing—review and editing, J.M., M.F., L.L.B., S.F., and T.V.; visualization, S.F., T.V., F.B., L.L.B., and M.G.; supervision, F.B., M.G., L.L.B., S.F., and T.V.; project administration, S.F. and T.V. All authors have read and agreed to the published version of the manuscript.

Funding: F.B. is partially funded by the National Plan for NRRP Complementary Investments (PNC, established with the decree law 6 May 2021, n. 59, converted by law n. 101 of 2021) in the call for the funding of research initiatives for technologies and innovative trajectories in the health and care sectors (Directorial Decree n. 931 of 6 June 2022)—project n. PNC0000003—Advanced Technologies for Human-Centred Medicine (project acronym: ANTHEM). This work reflects only the authors' views and opinions; neither the Ministry for University and Research nor the European Commission can be considered responsible for them.

Informed Consent Statement: Fully anonymized data. Informed consent was obtained from the subjects involved in the study.

Data Availability Statement: The data that support the findings of this study are available from the corresponding author upon reasonable request.

Acknowledgments: The authors would like to thank Bernardo Innocenti, at Université Libre de Bruxelles for providing the clinical images.

Conflicts of Interest: The authors declare no conflicts of interest.

Abbreviations

The following abbreviations are used in this manuscript:

AM	Additive Manufacturing
CT	Computed Tomography
FE	Finite Element
FI	Flare Index
HU	Hounsfield Unit
THA	Total Hip Arthroplasty
ρ^*	Relative Density
E	Elastic Modulus

References

1. Shichman, I.; Askew, N.; Habibi, A.; Nherera, L.; Macaulay, W.; Seyler, T.; Schwarzkopf, R. Projections and epidemiology of revision hip and knee arthroplasty in the United States to 2040–2060. *Arthroplast. Today* **2023**, *21*, 101152. [CrossRef]
2. W-Dahl, A.; Kärrholm, J.; Rogmark, C.; Nåtman, J.; Bülow, E.; Ighani Arani, P.; Mohaddes, M.; Rolfson, O. Swedish Hip Arthroplasty Register, Annual Report 2023. Available online: https://registercentrum.blob.core.windows.net/shpr/r/VGR_Annual-report_SHAR_2019_EN_Digital-pages_FINAL-ryxaMBUWZ_.pdf (accessed on 18 March 2024).
3. Torre, M.; Ceccarelli, S.; Cornacchia, A.; Carrani, E.; Ciccarelli, P.; Masciocchi, M. Registro Italiano Artroprotesi (RIAP), Report Annuale 2023. Available online: https://riap.iss.it/riap/it/attivita/report/2024/10/29/report-annuale-riap-2023/ (accessed on 5 November 2024).

4. Delaunay, C.; Hamadouche, M.; Girard, J.; Duhamel, A. What are the causes for failures of primary hip arthroplasties in France? *Clin. Orthop. Relat. Res.*® **2013**, *471*, 3863–3869. [CrossRef] [PubMed]
5. Heyland, M.; Checa, S.; Kendoff, D.; Duda, G.N. Anatomic grooved stem mitigates strain shielding compared to established total hip arthroplasty stem designs in finite-element models. *Sci. Rep.* **2019**, *9*, 482. [CrossRef]
6. Burchard, R.; Graw, J.A.; Soost, C.; Schmitt, J. Stress shielding effect after total hip arthroplasty varies between combinations of stem design and stiffness—A comparing biomechanical finite element analysis. *Int. Orthop.* **2023**, *47*, 1981–1987. [CrossRef]
7. Kheir, M.M.; Dilley, J.E.; Speybroeck, J.; Kuyl, E.V.; Ochenjele, G.; McLawhorn, A.S.; Meneghini, R.M. The influence of Dorr type and femoral fixation on outcomes following total hip arthroplasty for acute femoral neck fractures: A multicenter study. *J. Arthroplast.* **2023**, *38*, 719–725. [CrossRef]
8. Li, M.; Zeng, Y.; Nie, Y.; Liao, K.; Pei, F.; Yang, J.; Xie, H.; Shen, B. A high risk of postoperative periprosthetic femoral fracture in Dorr type C femurs: A retrospective cohort study with 10-year follow-up data and a preliminary monochromatic image analysis. *Int. J. Surg.* **2024**, *110*, 296–305. [CrossRef]
9. Wilkerson, J.; Fernando, N.D. Classifications in brief: The Dorr classification of femoral bone. *Clin. Orthop. Relat. Res.* **2020**, *478*, 1939–1944. [CrossRef]
10. Song, J.H.; Jo, W.L.; Lee, K.H.; Cho, Y.J.; Park, J.; Oh, S. Subsidence and perioperative periprosthetic fractures using collarless hydroxyapatite-coated stem for displaced femoral neck fractures according to Dorr type. *J. Orthop. Surg.* **2019**, *27*, 2309499019877530. [CrossRef] [PubMed]
11. Veldman, H.D.; Boymans, T.A.; van Steenbergen, L.N.; Heyligers, I.C. Age-associated changes in proximal femur morphology affect femoral component sizing in cementless hip arthroplasty. *Geriatr. Orthop. Surg. Rehabil.* **2022**, *13*, 21514593221144615. [CrossRef]
12. Zhen, P.; Liu, J.; Lu, H.; Chen, H.; Li, X.; Zhou, S. Primary total hip arthroplasty using an uncemented Wagner SL stem in elderly patients with Dorr type C femoral bone. *Int. Surg.* **2019**, *103*, 287–294. [CrossRef]
13. Lee, K.H.; Hung, Y.T.; Chang, C.Y.; Wang, J.C.; Tsai, S.W.; Chen, C.F.; Wu, P.K.; Chen, W.M. The cementless taper wedge vs. fit-and-fill stem in primary total hip arthroplasty: Risk of stem-related complication differs across Dorr types. *Arch. Orthop. Trauma Surg.* **2024**, *144*, 2839–2847. [CrossRef]
14. Abdullah, N.N.A.A.; Abdullah, A.H.; Ramlee, M.H. Current trend of lattice structures designed and analysis for porous hip implants: A short review. *Mater. Today Proc.* **2023**, *110*, 96–100. [CrossRef]
15. Seharing, A.; Azman, A.H.; Abdullah, S. A review on integration of lightweight gradient lattice structures in additive manufacturing parts. *Adv. Mech. Eng.* **2020**, *12*, 1687814020916951. [CrossRef]
16. Alkentar, R.; Kladovasilakis, N.; Tzetzis, D.; Mankovits, T. Effects of pore size parameters of titanium additively manufactured lattice structures on the osseointegration process in orthopedic applications: A comprehensive review. *Crystals* **2023**, *13*, 113. [CrossRef]
17. du Plessis, A.; Broeckhoven, C.; Yadroitsava, I.; Yadroitsev, I.; Hands, C.H.; Kunju, R.; Bhate, D. Beautiful and functional: A review of biomimetic design in additive manufacturing. *Addit. Manuf.* **2019**, *27*, 408–427. [CrossRef]
18. Ahmadi, S.; Campoli, G.; Amin Yavari, S.; Sajadi, B.; Wauthle, R.; Schrooten, J.; Weinans, H.; Zadpoor, A. Mechanical behavior of regular open-cell porous biomaterials made of diamond lattice unit cells. *J. Mech. Behav. Biomed. Mater.* **2014**, *34*, 106–115. [CrossRef] [PubMed]
19. Yan, C.; Hao, L.; Hussein, A.; Young, P. Ti–6Al–4V triply periodic minimal surface structures for bone implants fabricated via selective laser melting. *J. Mech. Behav. Biomed. Mater.* **2015**, *51*, 61–73. [CrossRef] [PubMed]
20. Arabnejad, S.; Burnett Johnston, R.; Pura, J.A.; Singh, B.; Tanzer, M.; Pasini, D. High-strength porous biomaterials for bone replacement: A strategy to assess the interplay between cell morphology, mechanical properties, bone ingrowth and manufacturing constraints. *Acta Biomater.* **2016**, *30*, 345–356. [CrossRef] [PubMed]
21. Melancon, D.; Bagheri, Z.; Johnston, R.; Liu, L.; Tanzer, M.; Pasini, D. Mechanical characterization of structurally porous biomaterials built via additive manufacturing: Experiments, predictive models, and design maps for load-bearing bone replacement implants. *Acta Biomater.* **2017**, *63*, 350–368. [CrossRef]
22. Zadpoor, A.A. Mechanical performance of additively manufactured meta-biomaterials. *Acta Biomater.* **2019**, *85*, 41–59. [CrossRef]
23. Meng, M.; Wang, J.; Huang, H.; Liu, X.; Zhang, J.; Li, Z. 3D printing metal implants in orthopedic surgery: Methods, applications and future prospects. *J. Orthop. Transl.* **2023**, *42*, 94–112. [CrossRef]
24. Kechagias, S.; Munford, M.J.; Masure, F.C.; van Arkel, R.J.; Oosterbeek, R.N. Lattice structures for bone replacement: The intersection of bone biomechanics, lattice design, and additive manufacturing. *Adv. Mater. Technol.* **2026**, *11*, e01885. [CrossRef]
25. Corona-Castuera, J.; Rodriguez-Delgado, D.; Henao, J.; Castro-Sandoval, J.C.; Poblano-Salas, C.A. Design and fabrication of a customized partial hip prosthesis employing CT-Scan data and lattice porous structures. *ACS Omega* **2021**, *6*, 6902–6913. [CrossRef]

26. McAnena, A.P.; McClennen, T.; Zheng, H. Patient-specific 3-dimensional-printed orthopedic implants and surgical devices are potential alternatives to conventional technology but require additional characterization. *CiOS Clin. Orthop. Surg.* **2025**, *17*, 1–15. [CrossRef]
27. Peto, M.; García-Ávila, J.; Rodriguez, C.A.; Siller, H.R.; da Silva, J.V.L.; Ramírez-Cedillo, E. Review on structural optimization techniques for additively manufactured implantable medical devices. *Front. Mech. Eng.* **2024**, *10*, 1353108. [CrossRef]
28. Jetté, B.; Brailovski, V.; Dumas, M.; Simoneau, C.; Terriault, P. Femoral stem incorporating a diamond cubic lattice structure: Design, manufacture and testing. *J. Mech. Behav. Biomed. Mater.* **2018**, *77*, 58–72. [CrossRef] [PubMed]
29. Jetté, B.; Brailovski, V.; Simoneau, C.; Dumas, M.; Terriault, P. Development and in vitro validation of a simplified numerical model for the design of a biomimetic femoral stem. *J. Mech. Behav. Biomed. Mater.* **2018**, *77*, 539–550. [CrossRef]
30. Izri, Z.; Bijanzad, A.; Torabnia, S.; Lazoglu, I. In silico evaluation of lattice designs for additively manufactured total hip implants. *Comput. Biol. Med.* **2022**, *144*, 105353. [CrossRef] [PubMed]
31. Alkhatib, S.E.; Tarlochan, F.; Mehboob, H.; Singh, R.; Kadirgama, K.; Harun, W.S.B.W. Finite element study of functionally graded porous femoral stems incorporating body-centered cubic structure. *Artif. Organs* **2019**, *43*, E152–E164. [CrossRef]
32. Nomura, J.; Takezawa, A.; Zhang, H.; Kitamura, M. Design optimization of functionally graded lattice infill total hip arthroplasty stem for stress shielding reduction. *Proc. Inst. Mech. Eng. Part H J. Eng. Med.* **2022**, *236*, 515–525. [CrossRef]
33. Gok, M.G. Creation and finite-element analysis of multi-lattice structure design in hip stem implant to reduce the stress shielding effect. *Proc. Inst. Mech. Eng. Part L J. Mater. Des. Appl.* **2022**, *236*, 429–439. [CrossRef]
34. Kladovasilakis, N.; Tsongas, K.; Tzetzis, D. Finite element analysis of orthopedic hip implant with functionally graded bioinspired lattice structures. *Biomimetics* **2020**, *5*, 44. [CrossRef]
35. Arabnejad, S.; Johnston, B.; Tanzer, M.; Pasini, D. Fully porous 3D printed titanium femoral stem to reduce stress shielding following total hip arthroplasty. *J. Orthop. Res.* **2017**, *35*, 1774–1783. [CrossRef]
36. Limmahakhun, S.; Oloyede, A.; Chantarapanich, N.; Jiamwatthanachai, P.; Sitthiseripratip, K.; Xiao, Y.; Yan, C. Alternative designs of load- sharing cobalt chromium graded femoral stems. *Mater. Today Commun.* **2017**, *12*, 1–10. [CrossRef]
37. Naghavi, S.A.; Tamaddon, M.; Garcia-Souto, P.; Moazen, M.; Taylor, S.; Hua, J.; Liu, C. A novel hybrid design and modelling of a customised graded Ti-6Al-4V porous hip implant to reduce stress shielding: An experimental and numerical analysis. *Front. Bioeng. Biotechnol.* **2023**, *11*, 1092361. [CrossRef]
38. Taddei, F.; Schileo, E.; Helgason, B.; Cristofolini, L.; Viceconti, M. The material mapping strategy influences the accuracy of CT-based finite element models of bones: An evaluation against experimental measurements. *Med. Eng. Phys.* **2007**, *29*, 973–979. [CrossRef]
39. Knowles, N.K.; Reeves, J.M.; Ferreira, L.M. Quantitative computed tomography (QCT) derived bone mineral density (BMD) in finite element studies: A review of the literature. *J. Exp. Orthop.* **2016**, *3*, 36. [CrossRef]
40. Yan, J.; Cheng, G.; Liu, S.; Liu, L. Comparison of prediction on effective elastic property and shape optimization of truss material with periodic microstructure. *Int. J. Mech. Sci.* **2006**, *48*, 400–413. [CrossRef]
41. Habib, C.; Kwon, Y.W.; Sachau, D.; Jung, A. Review and assessment of various lattice structure homogenization. *Multiscale Multidiscip. Model. Exp. Des.* **2026**, *9*, 55. [CrossRef]
42. Somnic, J.; Jo, B.W. Homogenization methods of lattice materials. *Encyclopedia* **2022**, *2*, 1091–1102. [CrossRef]
43. Hassani, B.; Hinton, E. A review of homogenization and topology optimization I—Homogenization theory for media with periodic structure. *Comput. Struct.* **1998**, *69*, 707–717. [CrossRef]
44. Hassani, B.; Hinton, E. A review of homogenization and topology opimization II—Analytical and numerical solution of homogenization equations. *Comput. Struct.* **1998**, *69*, 719–738. [CrossRef]
45. Gibson, L.J.; Ashby, M.F. The mechanics of three-dimensional cellular materials. *Proc. R. Soc. Lond. A* **1982**, *382*, 43–59. [CrossRef]
46. Gibson, L.J.; Ashby, M.F. *Cellular Solids*; Cambridge University Press: Cambridge, UK, 1997.
47. Behrens, B.A.; Wirth, C.; Windhagen, H.; Nolte, I.; Meyer-Lindenberg, A.; Bouguecha, A. Numerical investigations of stress shielding in total hip prostheses. *Proc. Inst. Mech. Eng. Part H J. Eng. Med.* **2008**, *222*, 593–600. [CrossRef] [PubMed]
48. Wang, Y.; Arabnejad, S.; Tanzer, M.; Pasini, D. Hip implant design with three-dimensional porous architecture of optimized graded density. *J. Mech. Des.* **2018**, *140*, 111406. [CrossRef]
49. Stolk, J.; Verdonschot, N.; Huiskes, R. Hip-joint and abductor-muscle forces adequately represent in vivo loading of a cemented total hip reconstruction. *J. Biomech.* **2001**, *34*, 917–926. [CrossRef] [PubMed]
50. Heller, M.O.; Bergmann, G.; Kassi, J.P.; Claes, L.; Haas, N.P.; Duda, G.N. Determination of muscle loading at the hip joint for use in pre-clinical testing. *J. Biomech.* **2005**, *38*, 1155–1163. [CrossRef]
51. Mehboob, H.; Ahmad, F.; Tarlochan, F.; Mehboob, A.; Chang, S.H. A comprehensive analysis of bio-inspired design of femoral stem on primary and secondary stabilities using mechanoregulatory algorithm. *Biomech. Model. Mechanobiol.* **2020**, *19*, 2213–2226. [CrossRef]
52. Frost, H. *The Laws of Bone Structure*; The Henry Ford Hospital Surgical Monographs; C.C. Thomas: Springfield, IL, USA, 1964.

53. Weinans, H.; Huiskes, R.; Grootenboer, H.J. Effects of material properties of femoral hip components on bone remodeling. *J. Orthop. Res.* **1992**, *10*, 845–853. [CrossRef]
54. Morgan, E.F.; Unnikrisnan, G.U.; Hussein, A.I. Bone mechanical properties in healthy and diseased states. *Annu. Rev. Biomed. Eng.* **2018**, *20*, 119–143. [CrossRef]
55. Polo, S.; García-Domínguez, A.; Rubio, E.M.; Claver, J. Lattice Structures in additive manufacturing for biomedical applications: A systematic review. *Polymers* **2025**, *17*, 2285. [CrossRef]
56. Delikanli, Y.E.; Kayacan, M.C. Design, manufacture, and fatigue analysis of lightweight hip implants. *J. Appl. Biomater. Funct. Mater.* **2019**, *17*, 2280800019836830. [CrossRef] [PubMed]
57. Barba, D.; Alabort, E.; Reed, R. Synthetic bone: Design by additive manufacturing. *Acta Biomater.* **2019**, *97*, 637–656. [CrossRef] [PubMed]
58. Al-Husinat, L.; Jouryyeh, B.; Al Sharie, S.; Al Modanat, Z.; Jurieh, A.; Al Hseinat, L.; Varrassi, G. Bone cement and its anesthetic complications: A narrative review. *J. Clin. Med.* **2023**, *12*, 2105. [CrossRef] [PubMed]
59. Schwarzkopf, E.; Sachdev, R.; Flynn, J.; Boddapati, V.; Padilla, R.E.; Prince, D.E. Occurrence, risk factors, and outcomes of bone cement implantation syndrome after hemi and total hip arthroplasty in cancer patients. *J. Surg. Oncol.* **2019**, *120*, 1008–1015. [CrossRef]
60. Lan, P.; Chen, X.; Fang, Z.; Zhang, J.; Liu, S.; Liu, Y. Effects of comorbidities on pain and function after total hip arthroplasty. *Front. Surg.* **2022**, *9*, 829303. [CrossRef]
61. Huiskes, R.; Weinans, H.; Grootenboer, H.; Dalstra, M.; Fudala, B.; Slooff, T. Adaptive bone-remodeling theory applied to prosthetic-design analysis. *J. Biomech.* **1987**, *20*, 1135–1150. . [CrossRef]